



HAL
open science

Dynamics of the high-latitude ionospheric irregularities during the 17 March 2015 St. Patrick's Day storm: Ground-based GPS measurements

Iurii Cherniak, Irina Zakharenkova, Robert J. Redmon

► **To cite this version:**

Iurii Cherniak, Irina Zakharenkova, Robert J. Redmon. Dynamics of the high-latitude ionospheric irregularities during the 17 March 2015 St. Patrick's Day storm: Ground-based GPS measurements. *Space Weather: The International Journal of Research and Applications*, 2015, 13, pp.585-597. 10.1002/2015SW001237 . insu-03579556

HAL Id: insu-03579556

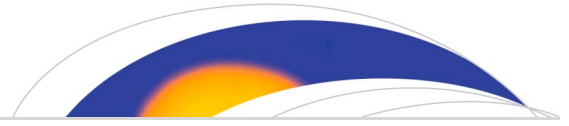
<https://insu.hal.science/insu-03579556>

Submitted on 18 Feb 2022

HAL is a multi-disciplinary open access archive for the deposit and dissemination of scientific research documents, whether they are published or not. The documents may come from teaching and research institutions in France or abroad, or from public or private research centers.

L'archive ouverte pluridisciplinaire **HAL**, est destinée au dépôt et à la diffusion de documents scientifiques de niveau recherche, publiés ou non, émanant des établissements d'enseignement et de recherche français ou étrangers, des laboratoires publics ou privés.

Copyright



RESEARCH ARTICLE

10.1002/2015SW001237

Key Points:

- Multisite GPS observations are used to study the irregularities dynamics
- Strong irregularities related to the formation of storm enhanced density and tongues of ionization
- Irregularities intensity and dynamics are correlated with hemispheric power index

Supporting Information:

- Readme
- Movie S1
- Movie S2
- Movie S3
- Movie S4

Correspondence to:

I. Cherniak,
tcherniak@ukr.net

Citation:

Cherniak, I., I. Zakharenkova, and R. J. Redmon (2015), Dynamics of the high-latitude ionospheric irregularities during the 17 March 2015 St. Patrick's Day storm: Ground-based GPS measurements, *Space Weather*, 13, 585–597, doi:10.1002/2015SW001237.

Received 10 JUN 2015

Accepted 18 AUG 2015

Accepted article online 21 AUG 2015

Published online 25 SEP 2015

Dynamics of the high-latitude ionospheric irregularities during the 17 March 2015 St. Patrick's Day storm: Ground-based GPS measurements

Iurii Cherniak¹, Irina Zakharenkova^{1,2}, and Robert J. Redmon³

¹Space Radio-Diagnostic Research Center, University of Warmia and Mazury, Olsztyn, Poland, ²Institut de Physique du Globe de Paris, Paris, France, ³National Centers for Environmental Information, National Oceanic and Atmospheric Administration, Boulder, Colorado, USA

Abstract We report first results on the study of the high-latitude ionospheric irregularities observed in worldwide GPS data during the St. Patrick's Day geomagnetic storm (17 March 2015). Multisite GPS observations from more than 2500 ground-based GPS stations were used to analyze the dynamics of the ionospheric irregularities in the Northern and Southern Hemispheres. The most intense ionospheric irregularities lasted for more than 24 h starting at 07 UT of 17 March. This period correlates well with an increase of the auroral Hemispheric Power index. We find hemispheric asymmetries in the intensity and spatial structure of the ionospheric irregularities. Over North America, the ionospheric irregularities zone expanded equatorward below ~45°N geographic latitude. Additionally, the strong midlatitude and high-latitude GPS phase irregularities in the auroral oval were found to be related to the formation of storm enhanced density and deepening of the main ionospheric trough through upper atmosphere ionization by energetic particle precipitation. Significant increases in the intensity of the irregularities within the polar cap region of both hemispheres were associated with the formation and evolution of the storm enhanced density/tongue of ionization structures and polar patches.

1. Introduction

The most intense ionospheric irregularities have been observed during ionospheric storms, resulting from significant increases in auroral particle precipitation and high-latitude ionospheric electric fields and currents lasting several hours or more during magnetospheric disturbances [e.g., *Phelps and Sagalyn*, 1976; *Keskinen and Ossakow*, 1983; *Tsunoda*, 1988]. Auroral particle precipitation creates highly structured enhancements of the ionospheric plasma density. Such ionospheric irregularities occurring during strong geomagnetic storms can cause rapid phase fluctuations in Global Positioning System (GPS) signals. Today, the GPS-based technique is a proven method for detection and near real-time monitoring of the occurrence and dynamics of ionospheric irregularities [e.g., *Aarons*, 1997; *Pi et al.*, 1997; *Jakowski et al.*, 2005; *Coster and Komjathy*, 2008; *Kintner et al.*, 2007; *Smith et al.*, 2008; *Prikryl et al.*, 2010; *Tiwari et al.*, 2013; *Cherniak et al.*, 2014a]. Our earlier results on GPS data analysis during geomagnetic storms reveal that the major features of the irregularity pattern are the intensity of the GPS-based Rate of TEC (total electron content) index (ROTI) and the position of the irregularity oval's equatorial border [*Cherniak et al.*, 2014b].

In this paper, we report the features of the intense ionospheric irregularities occurring during the St. Patrick's Day storm of 17 March 2015. This storm is the largest geomagnetic storm since the beginning of the 24th solar cycle. We collected and processed data from several global and regional ground-based GPS networks. More than 2500 stations were involved in the analysis. To detect the high-latitude ionospheric irregularities, we used the Rate of TEC (ROT) and ROTI estimates to study the occurrence of TEC fluctuations [*Pi et al.*, 1997]. The ROTI maps allow us to estimate the overall fluctuation activity and the dynamics of the ionospheric irregularities.

2. Space Weather Conditions During the St. Patrick's Day Geomagnetic Storm

This disturbance in the ionosphere-plasmasphere-magnetosphere system was the result of a severe geomagnetic storm (G4 level) occurring on 17 March 2015. The Earth-directed coronal mass ejection produced by the long duration C9 solar flare arrived at the Earth magnetosphere and led to the sudden

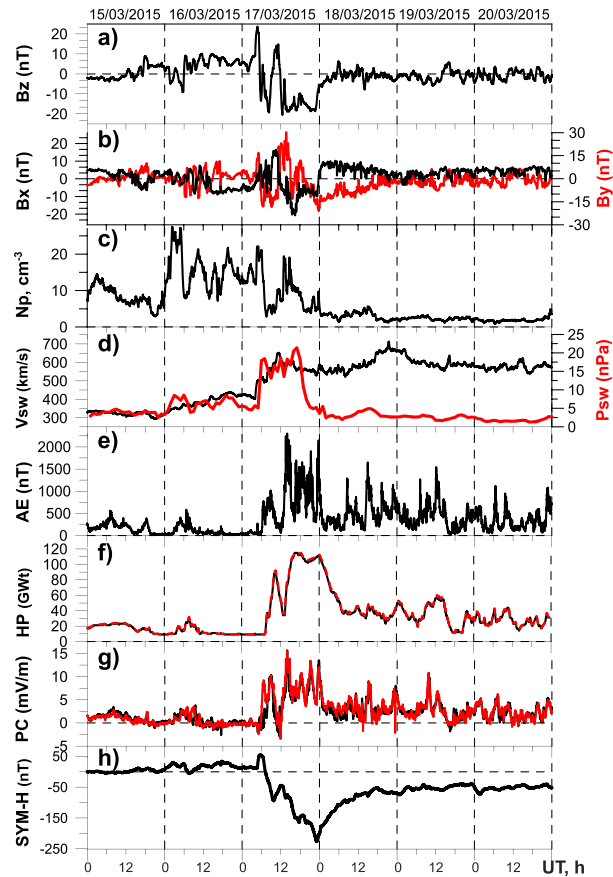


Figure 1. Geomagnetic conditions on 15–20 March 2015: IMF (a) B_z , (b) B_x and B_y components (Geocentric Solar Magnetospheric), (c) density, (d) velocity and dynamic pressure of the solar wind, and the (e) auroral electrojet (AE), (f) Hemispheric Power (HP), (g) Polar Cap (PC) indices for the Northern (black) and Southern (red) Hemispheres, and (h) SYM-H indices. We do not time shift the OMNI data.

~14 UT. Between these two peaks, a northward turning of B_z was observed. Also, we use the NOAA Hemispheric Power (HP) index, which estimates the power in gigawatts (GW) deposited in the polar regions by precipitating auroral energetic particles. The HP index increases strongly just after SSC and its behavior is correlated with solar wind pressure, AE, and SYM-H variations. The midlatitude magnetic activity index K_p (not shown) reached the value of 8. There was also an increase in the solar wind speed and dynamic pressure together with an IMF rotation before the main phase. These premain phase processes lead to a short-term ionospheric disturbance on 16 March and the subsequent development of the plasma density irregularities in the ionosphere.

The strong disturbance of the geomagnetic field on 17 March 2015 led to intense particle precipitation and an enhancement in substorm activity. It was reported that during 17–18 March 2015 aurora was observed at different locations around the globe, even at midlatitudes as equatorward as Tasmania and New Zealand in the Southern Hemisphere as well as in the United States, Europe, and Japan in the Northern Hemisphere [e.g., Nishitani et al., 2015; Kamide and Kusano, 2015; GUVI TIMED JHU/APL website, 2015, <http://guvitimed.jhuapl.edu>; U.S. Geological Survey [2015], NGP website <http://geomag.usgs.gov/storm/22>, and links therein]. For this case, the authors also analyzed the ionograms of the ground-based ionosonde networks (not shown) and found a considerable increase in absorption at Northern Hemisphere midlatitudes associated with expanded auroral particle precipitation. Such severe storming resulted in significant consequences on satellite operations, radio wave propagation, and Global Navigation Satellite Systems (GNSS)-related services and applications. The effects of the severe geomagnetic “Halloween Storm” event in October 2003 on the

storm commencement that was registered on 17 March 2015 at 0445 UT. A sudden increase in the solar wind and interplanetary magnetic field (IMF) parameters was recorded by the Advanced Composition Explorer satellite’s payload (see Figures 1a–1d). On 17 March, the solar wind speed increased from 400 to 650 km/s. During the following days, the solar wind speed varied within 500–650 km/s. Kamide and Kusano [2015] reported that this severe geomagnetic storm resulted from the superposition of two successive moderate storms driven by two successive southward IMF structures.

Figure 1a shows the variability of the IMF B_z component. After the shock arrival, the northward IMF B_z component reached the value of ~25 nT. At ~0530 UT, the IMF B_z turned southward and reached the first minimum value of –18 nT at 0615 UT. Then the IMF B_z sharply turned northward and varied drastically between north and south over ~8 h. After ~1340 UT, the B_z turned southward again and remained southward directed until the end of this day. The SYM-H index reached two local minima of –93 and –150 nT at 0940 and 1630 UT, respectively. The minimum of the SYM-H index of –226 nT occurred at 23 UT.

The auroral activity index AE and Polar Cap (PC) index indicate the presence of two intensification peaks at ~09 UT and

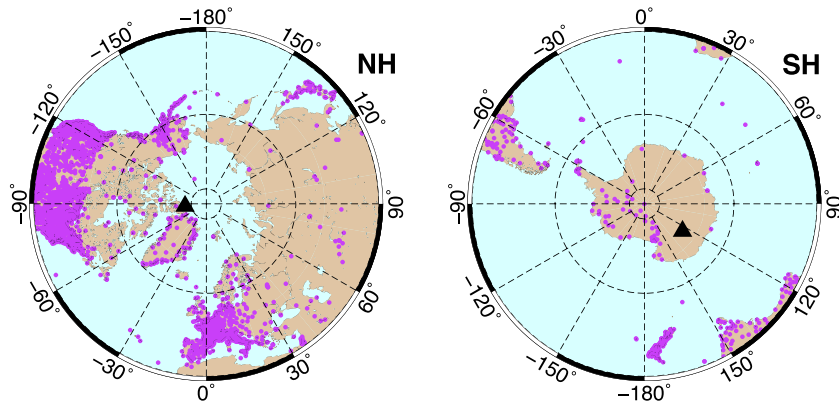


Figure 2. Location of the used GPS permanent stations in geographic coordinates (polar projection). Black triangles indicate the position of the corrected geomagnetic poles.

differential GPS positioning and Wide Area Augmentation Service (WAAS) systems was studied in detail by Skone and Yousuf [2007]. The statistics of the GPS Loss of Lock on a global scale during four geomagnetic storms of the 23th solar cycle was also estimated in Astafyeva *et al.* [2014]. For the 17 March 2015 storm, the degradation of positioning performance was also reported by the WAAS Test Team [Wanner, 2015].

3. Data and Methodology

In this study, we made use of raw GPS measurements provided by ground-based networks of GPS receivers. Here we considered the polar, subauroral, and midlatitude regions of the Northern and Southern Hemispheres, from 30° geomagnetic latitude to the poles. These regions are covered by permanent GNSS stations of the International GNSS Service (IGS), University NAVSTAR Consortium (UNAVCO), Continuously Operating Reference Stations (CORS), and European Reference Frame Permanent Network (EPN) and complemented by several regional networks located in Australia, New Zealand, Argentina, and Canada. We note significant progress in the evolution of the global/regional GPS networks, especially in the high-latitude region. In total, these networks provide much better spatial coverage than was accessible during storms and superstorms of the 23rd solar cycle. We have a unique opportunity to use this expanded GPS network to examine the largest storm since the beginning of the new cycle.

Of the available 3500 permanent worldwide stations, we excluded the equatorial and low-latitude stations to yield ~2500 and ~180 stations for the Northern and Southern Hemispheres, respectively. Figure 2 presents the geographical location of the available GPS stations for both hemispheres. All raw Receiver Independent Exchange Format data were resampled to 30 s resolution. We processed GPS measurements to obtain several GPS-based parameters. We calculated slant total electron content (TEC) values from the frequency-differenced GPS phase delay [e.g., Blewitt, 1990]. We used the ROT as a measure of phase fluctuation activity and the ROTI as a GPS-based index that characterizes the severity of the GPS phase fluctuations and detects the presence of ionospheric irregularities, and measures the irregular structures of TEC spatial gradients [Pi *et al.*, 1997].

In order to calculate ROT, the algorithm was applied to the slant TEC estimates (equation (1))

$$ROT = \frac{TEC_k^i - TEC_{k-1}^i}{(t_k - t_{k-1})} \quad (1)$$

where i is a GPS satellite and t_k is an epoch time. ROT is calculated in units of total electron content unit (TECU)/min for each visible GPS satellite over a permanent ground-based GPS station. One TECU equals 10^{16} el/m². The ROT values were calculated for all visible GPS satellites for elevation angles over 30°. Then, the ROT data were detrended and used to obtain the ROTI values as a standard deviation with a running window of 5 min (equation (2))

$$ROTI = \sqrt{\langle ROT^2 \rangle - \langle ROT \rangle^2} \quad (2)$$

To retrieve specific features of the dynamics of the ionospheric irregularities, the multisite GPS database was processed by utilizing several techniques. We analyzed the diurnal ROTI polar maps to develop an overall

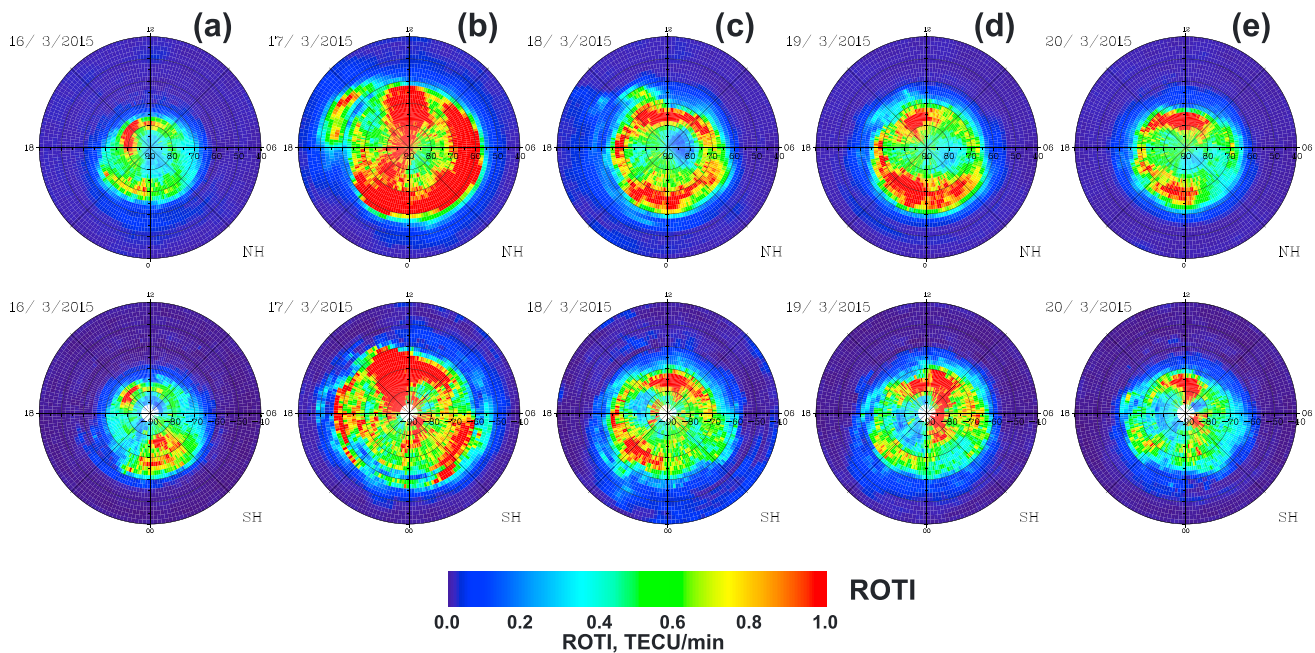


Figure 3. (a–e) Diurnal ROTI maps in corrected geomagnetic coordinates for the Northern and Southern Hemispheres (indicated as NH and SH, respectively) for 16–20 March 2015. Polar view map covers 00–24 MLT and 40°–90° MLAT. In each map, magnetic noon/midnight is at the top/bottom.

representation of the high-latitude irregularities including their spatial evolutions and linkage with the Earth’s magnetosphere (due to strong connections between the Earth’s magnetic field and the ionosphere). The ROTI mapping technique is described in detail by *Cherniak et al.* [2014a, 2014b]. Here ROTI behavior is represented as a function of magnetic local time (MLT) and corrected magnetic latitude (MLAT) for a specific day. We use the corrected geomagnetic (CGM) coordinates with the Definitive/International Geomagnetic Reference Field models. The resultant polar map is a daily map with a 00–24 MLT time frame and a magnetic latitude range of 40°–90°. ROTI data were binned and averaged in cells of 2° magnetic latitude by 8 min MLT, i.e., the map resolution is 25 cells along the MLAT axis and 180 cells along the MLT axis.

The second approach was implemented to estimate the global dynamics of the ionospheric irregularities during the main and recovery phases of the geomagnetic storm. We created and analyzed polar ROTI maps in geographical coordinates for both hemispheres. Large ROTI values correspond to an increased probability of phase fluctuations of the GPS signal. The fluctuations occur when the radio signals pass through plasma density irregularities in the ionosphere. The value in every cell is calculated by averaging all ROTI values within this cell area, and it is proportional to the fluctuation event probability in the current sector.

The third approach was based on the detailed analysis of the ROT variability along passes of all visible satellites over a GPS station. We considered ROT values for a selected chain of GPS stations in the European, North American, and Australian sectors. The ROT variability with a 30 s temporal resolution allows us to identify the temporal dependencies of the occurrence of ionospheric irregularities and their intensity against changes in the space weather parameters.

4. Results

Three types of the GPS data processing were implemented to analyze the dynamics of the high-latitude ionospheric irregularities produced by the St. Patrick’s Day geomagnetic storm.

4.1. Diurnal ROTI Maps

Figure 3 presents the diurnal ROTI maps for the Northern and Southern Hemispheres in magnetic coordinates. For the relatively quiet day of 16 March (see Figure 3a), the position of the irregularities oval is within 75° MLAT and the ROTI values have their peak intensity around 14–16 MLT in both hemispheres. An increase in the occurrence of irregularities was also observed within 65°–70° MLAT in the premidnight sector for the

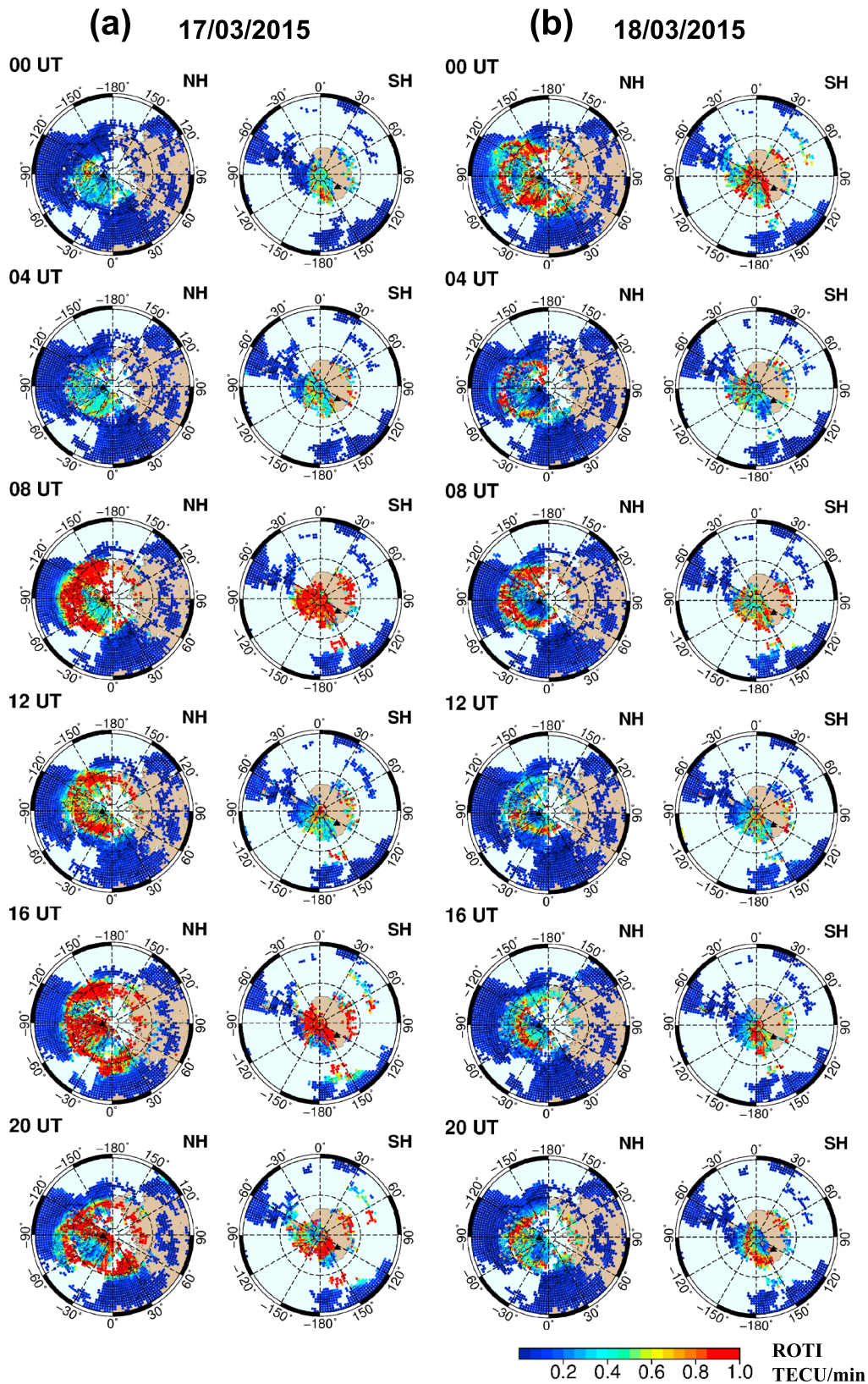


Figure 4. Hourly ROTI maps over the Northern and Southern Hemispheres in geographical projections. Each vertical panel represents sequence of ROTI maps for (a) 17 March and (b) 18 March. Polar view map covers the geographical longitude range of -180° to 180° and latitude range of 30° – 90° . Dashed lines represent the grid at every 30° of latitude/longitude. Black triangles indicate the position of the magnetic poles in corrected geomagnetic coordinates.

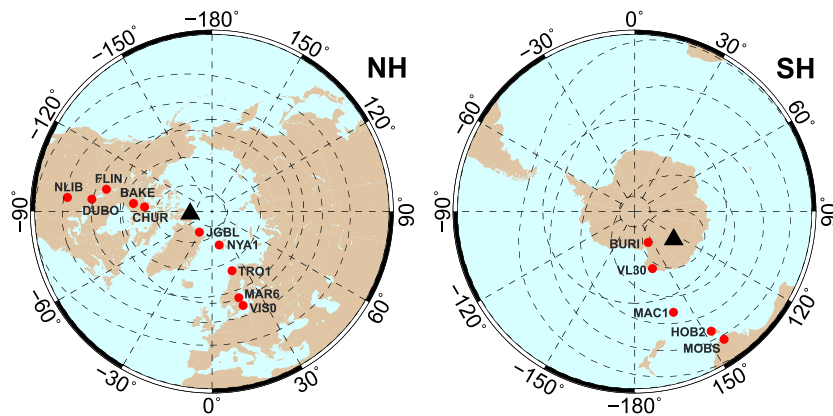


Figure 5. Chains of the selected GPS stations in the North American, European, and Antarctica-Australian sectors. Dashed lines show the isolines of 50°, 60°, 70°, and 80° MLAT, and black triangles indicate the position of the magnetic poles in corrected geomagnetic coordinates.

Northern Hemisphere and in the postmidnight sector for the Southern Hemisphere. Most probably, it was initiated by an increase in the solar wind speed and pressure on the magnetosphere together with rotation of the IMF. The resultant particle precipitation, implied by the heightened *HP* index (see Figure 1f), intensified the occurrence of ionospheric irregularities near and in the auroral region.

During the main phase of the storm (0445–2300 UT), a series of substorms occurred starting at ~06 UT. These substorms resulted in the development of enhanced auroral activity, increased visible discrete aurora, and a persistence of strong ionospheric irregularities. The diurnal ROTI map corresponding to the most disturbed day of 17 March 2015 (see Figure 3b) shows dramatic changes in the pattern of the high-latitude ionospheric plasma irregularities. A significant increase of the ROTI intensity was accompanied by an expansion of the equatorial border of the irregularities oval (to ~55° MLAT). This pattern of the ionospheric response was observed in both hemispheres, but with some differences. In the Northern Hemisphere, the most intense ionospheric irregularities were found within 60°–70° MLAT during ~20–09 MLT and one noontime peak was observed at ~11–13 MLT. Distinctly separated maxima of the irregularities intensity can be found within 50°–60° MLAT at ~15–17 MLT. In the Southern Hemisphere, there are two intense maxima along the oval: one nighttime maximum at ~04–06 MLT and one in the noon sector at ~09–15 MLT.

4.2. Hourly ROTI Maps

Figure 4 shows hourly ROTI maps in geographic projections for 17–18 March 2015 at specific UTs. The full sequence of the hourly maps is available in Movies S1–S4 of the study’s supporting information. These hourly ROTI maps demonstrate the dynamics of the ionospheric irregularities in a geographic view. The map for 00 UT means that here we averaged data from 0000 to 0059 UT. The dramatic changes of the irregularities pattern start after 07–08 UT on 17 March, initiated by the intensification of auroral activity (see *AE* and *HP* indices in Figures 1e and 1f). The most intense irregularities corresponded to very high ROTI values (greater than or equal to 1 TECU/min) and were found to form an oval-like structure around the geomagnetic pole. It was more obvious for the Northern Hemisphere. The GPS-detected irregularity oval expanded equatorward during several hours, and its equatorial edge was detected in the North American sector at ~45–50°N latitude for more than 6 h. It is necessary to note that the North American region has better data coverage, and the hourly ROTI maps provide their best resolution in this region. This elongated formation mainly occurred over North America, and it appeared as the separated daytime maximum (50°–60° MLAT) in the diurnal ROTI map (see Figure 3b, top). Intensification and expansion of the irregularity zone toward midlatitudes was also seen over the Southern Hemisphere. But due to the poorer coverage of GPS data over this region, such effects were observed in the longitude range of 30°E–180°E (over GPS stations of the New Zealand and Australia networks and islands in the Pacific Ocean).

4.3. High-Resolution ROT Variability for Selected GPS Station Chains

For further analysis, we traced the dependency of the ionospheric irregularities occurrence on auroral activity with higher temporal resolution. Here we considered three north-south chains of GPS stations over North

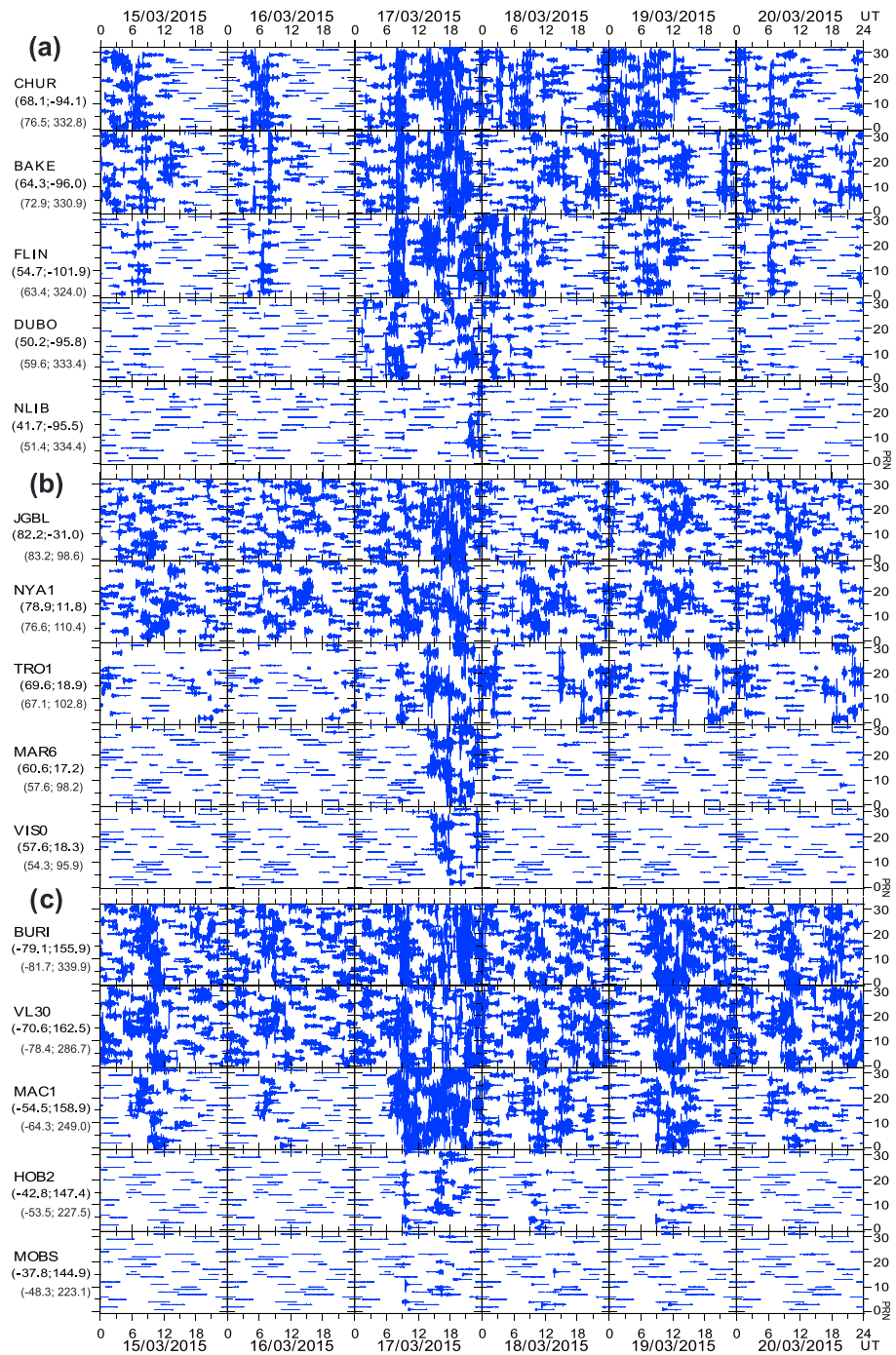


Figure 6. Variability of ROT values along satellite passes over chain of selected GPS stations: (a) the North American sector, (b) the European sector, and (c) the Antarctica-Australian sector. Right vertical axis shows the PRN (pseudo random noise) satellite number. Labels on the vertical axis indicate the station name, its geographical (first line below name) and geomagnetic coordinates.

America, Europe, and Australia (see Figure 5). Figure 6 presents the ROT variability, induced by GPS signal fluctuations, for visible satellites over selected GPS stations. During the first particle precipitation event with *HP* peaking within 07–09 UT, we can see intensification of the GPS fluctuations at all sectors. However, for the Northern Hemisphere we found different intensities over America and Europe. GPS fluctuations in America were much more intensive and were observed for all stations from the polar region down to 60° MLAT.

Over Europe, this effect was rather weak and was observed at two stations above 65° MLAT. This difference can be caused by European stations that were in the morning sector, as the most intense fluxes of precipitating particles come from the nightside magnetosphere. Decreases in GPS fluctuation activity was observed by all stations near 10–12 UT, corresponding to the sudden minimum of *HP*. After 13 UT, a new series of GPS fluctuations started. In both hemispheres, the zone with strong GPS fluctuations expanded equatorward and included the GPS stations located as equatorward as 50° MLAT.

During the recovery phase of the storm, lasting for several days, the auroral activity persisted (see *AE*, *HP* in Figures 1e and 1f). The diurnal ROTI maps indicate the presence of ionospheric irregularities but with lower magnitudes (see Figures 3c and 3d). The irregularities oval shifted poleward and its equatorial border was not observed below 60° MLAT. For these days, ROT values for GPS station chains indicated a gradual decrease of the irregularity intensity and a disappearance of the GPS fluctuations over stations located below 55° MLAT (see Figure 6). However, the GPS fluctuations were observed for GPS stations above 60° MLAT at both hemispheres during 18–20 March 2015.

5. Discussion

The periods of the most intense irregularity occurrences in GPS data coincided with strong increases in the auroral *HP* index. The Hemispheric Power index is often used as a measure of auroral particle precipitation activity [Fuller-Rowell and Evans, 1987; Emery *et al.*, 2008; Newell *et al.*, 2009]. The present study uses the *HP* index produced by the NOAA Space Weather Prediction Center (SWPC), which is calculated using the Oval Variation, Assessment, Tracking, Intensity and Online Nowcasting (OVATION) Prime empirical model [Newell *et al.*, 2009, 2010]. The version of the OVATION Prime model used in this study was built on roughly two decades of precipitating particle observations collected by the Defense Meteorological Satellite Program (DMSP) spacecraft. The DMSP particle detectors used in the model development point toward local zenith and thus for the case of an extremely expanded auroral oval, the OVATION Prime derived *HP* index is likely an underestimate (R. Viereck, private communication, 2015). OVATION Prime uses solar wind observations via the Newell *et al.* [2007] solar wind coupling function (a measure of dayside magnetic merging) to predict the intensity and characteristic energy of diffuse and discrete precipitating particle spectra. Due to the high temporal resolution of the *HP* estimate, we can correlate the occurrence of GPS-detected ionospheric irregularities with particle precipitation. The *HP* estimates were about 10 GW before 0650 UT. After 0650 UT, *HP* started to rise and quickly reached ~40 GW at 0730 UT and first peaked at a value of 90 GW at 0940 UT. Dynamics of the ionospheric irregularities intensity were found to follow these *HP* changes. The first rapid increase of the irregularity intensity with the equatorward expansion of this zone was shown in the hourly ROTI map of 06 UT (see Movie S2). During 07–09 UT, the zones of intense irregularities (ROTI values equal to 1 TECU/min and higher) extended equatorward in both hemispheres and for the first time during this storm the equatorial border of this zone reached 45°N (MLAT) in the North American sector in the ROTI map for 09 UT. After that, the intensity of the irregularities started to decrease until 13 UT, which corresponded to a decrease in *HP* down to 35 GW near 1230 UT. This decrease was initiated by the northward turn of the IMF B_z . After 13 UT, the *HP* values started to rise again and reached the peak of 116 GW near 16 UT. Subsequently, *HP* values exceeding 100 GW persisted for about 10 h until 0130 UT of 18 March. Within the very same period, we observed the second series of significant intensification of the irregularities structures detected in GPS data over both hemispheres. Despite data coverage limits in the Southern Hemisphere, we can still recognize features of hemispheric asymmetries during this time.

The intense irregularities observed in the diurnal and hourly ROTI maps can be explained by the significant storm-induced gradients of the ionospheric plasma density, both caused by auroral particle precipitation and plasma flows. In the midlatitude and high-latitude ionosphere, there are several sources of large-scale plasma gradients such as ionization of the neutral component by energetic particles, the formation of a storm enhanced density (SED) and the evolution of a SED plume into a polar tongue of ionization (TOI), and the development of the midlatitude ionospheric trough. A SED has been described as a spatially narrow, distinct, region of enhanced plasma density (plume) observed in the postnoon and premidnight sectors extending from the equatorward edge of the main ionospheric trough to the noon time cusp [Foster, 1993; Coster *et al.*, 2007]. The evolution and dynamics of the SED can be successfully monitored with the high-resolution GPS TEC maps [Coster *et al.*, 2007; Coster and Skone, 2009]. The dayside source of the TOI is the SED plume

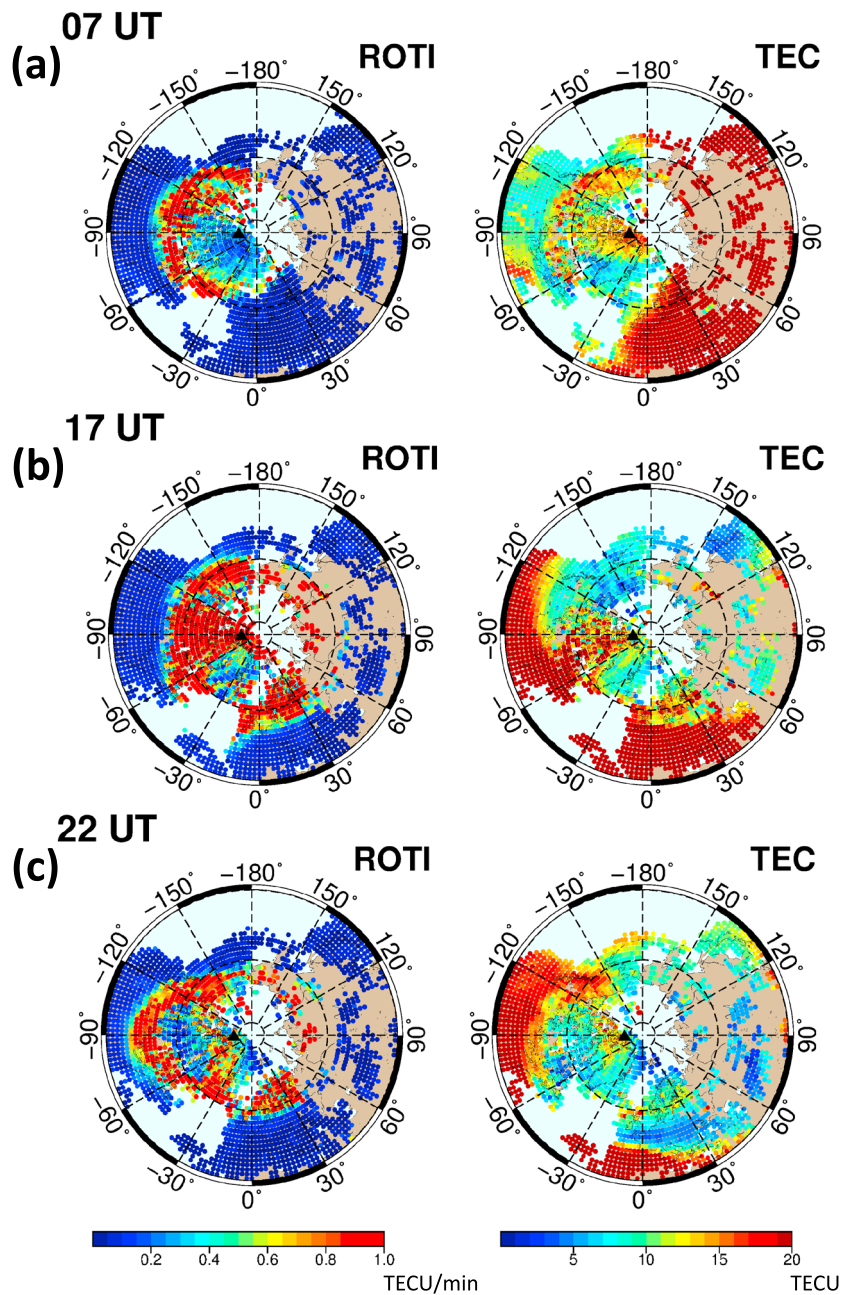


Figure 7. Concurrent observations of GPS ROTI and GPS TEC over the Northern Hemisphere for selected moments of time: (a) 07 UT, (b) 17 UT, and (c) 22 UT of 17 March 2015. The geographic latitude range is 30°N to 90°N.

transported from lower latitudes in the postnoon sector by the subauroral disturbance electric field. These subauroral electric fields and plasma flows are specific phenomena determined by *Foster and Burke* [2002] as subauroral polarization streams. Antisunward convection carries this material through the dayside cusp and across the polar cap to the nightside where the auroral *F* region is significantly enhanced by the SED material [Foster et al., 2005]. During the SED/TOI convection across the polar cap, there occurs a fragmentation of the TOI into discrete polar cap patches [e.g., Sojka et al., 1993]. A polar cap patch typically has a density that is 2–20 times larger than the surrounding background electron density, and its horizontal size ranges from 100 to 1000 km [e.g., Tsunoda, 1988; Crowley et al., 2000]. They can be successfully observed in GPS measurements due to the steep density gradients and irregularities developed at their boundaries.

In the hourly maps for the Northern Hemisphere (see Figure 4), we observe radial-oriented structures in the day-night direction. These structures can be associated with the formation of the SED/TOI structures and their further transformation into large-scale polar cap patches, which follow the convection pattern antisunward across the polar cap. Figure 3b confirms the presence of the TOI structures occurring in the postnoon sector in both hemispheres. This signature was observed from 13 UT on 17 March 2015 to 02 UT on 18 March 2015 (see supporting information Movies S2 and S3). The SED/TOI structure rotated from 90°W through 120°W to 150°W longitude as the dayside cusp moved. The intensity of SED/TOI-related ionospheric irregularities was decreased after 22 UT on 17 March.

As additional support, we further processed GPS data to estimate the absolute values of the vertical GPS TEC. We processed GPS data for the Northern Hemisphere due to the much better coverage by the GPS stations. We used the same choice of the elevation cutoff angle (30°) as for ROT/ROTI calculations. The algorithm used is described in *Blewitt* [1990] and *Zakharenkova et al.* [2014]. The slant TEC was calibrated from the instrumental biases. The differential code biases for GPS satellites were used from the CODE (Center for Orbit Determination in Europe) biases product. Receiver biases for GPS stations were estimated inside the algorithm processing. We constructed the TEC maps with TEC values binned into 2° x 2° geographic latitude/longitude cells.

Figure 7 illustrates the concurrent observations of the GPS ROTI and GPS TEC for the three most interesting cases. The first case corresponds to the first increase of auroral activity at 07 UT (see Figure 7a). Here the North American region is in the late evening and night local time sector (~01 MLT for mid-North America), and we found the first strong intensification of the GPS ROTI over this region with the equatorward expansion. Figure 7a (right) shows the GPS TEC map. The main ionospheric trough is clearly detected near 45°N. Even more interesting is the occurrence of the zone with increased density at the poleward edge of the trough. This zone is observed at 50°–70°N, and its location coincides well with the position of the most intense GPS irregularities in the ROTI map (left graph). We can conclude that, for this case, the GPS irregularities were due to plasma density gradients caused by storm-induced particle precipitation and their subsequent ionization of the neutral species. The enhancement of energetic particle precipitation within the auroral oval and ion convection results in more plasma being accumulated at the poleward edge of the trough by direct ionization as well as transport [*Tsunoda*, 1988; *Rodger et al.*, 1992] and makes the poleward edges of the trough steeper [*Kersley et al.*, 1997]. So increases in particle precipitation at the beginning of the storm's main phase most probably lead to the formation of the large-scale ionospheric plasma enhancements at the poleward edge of the trough and the steeper poleward wall of the trough in the nightside ionosphere.

Figure 7b shows ROTI and TEC for 17 UT shortly after the second intensification in auroral activity (see *AE* and *HP* in Figure 1) as well as in the *PC* index (Figure 1). Here we observe more complicated behaviors in both GPS ROTI and TEC. In the GPS TEC map (right column), we observe the beginning of the main trough formation at 55°N over the European sector and irregular formations of the plasma density enhancements in the area of its poleward edge. The North American region moved to the dayside local time sector. The dayside TEC enhancement was observed below 45°N. The formation of the SED/TOI structures is revealed in the longitude range of 60°W–90°W. The latitude extent of the SED/TOI plasma density enhancement reached the north magnetic pole. The GPS ROTI map shows the occurrence of ionospheric irregularities at the poleward edge of the main trough. The most intense ROTI variations corresponded to GPS signal phase fluctuations caused by the structured ionospheric plasma inside the auroral oval from 08 UT to 15 UT when the SED/TOI structure started its development.

For the third case of 22 UT (see Figure 7c), we can see the further deepening and equatorward extension of the main trough over the European region, as well as plasma density enhancements near 55°–70°N. For the North American region, the storm-induced TEC behavior was observed with TEC enhancements below middle latitudes and TEC decreases at the high latitudes. The large-scale SED structure was found within the 60°W–120°W longitude range. The well-recognized TOI structure had a poleward direction extending in longitude to 150°W. The discrete polar patches with different intensity can be found close to the magnetic pole within the area of 80°–85°N latitude and 60°W–120°W longitude. The GPS ROTI map represents well the development of the discussed TEC irregularities. We want to emphasize that the observed expansion of the GPS-detected irregularities oval equatorward to ~45°–50°N latitude (seen also in Figure 3b, top) was related to the SED structure formation in the Western Hemisphere (radial-oriented structures from local noon to midnight) as well as auroral oval development in the Eastern Hemisphere.

We should also note that this geomagnetic storm occurred close to the equinox, so we do not expect pronounced seasonal (summer/winter) effects in the form of interhemispheric differences in particle precipitation activity [e.g., Emery *et al.*, 2008]. However, features of the ionospheric response to the auroral activity differ in both hemispheres.

The asymmetry can be explained in part by the IMF orientation which can have a strong impact on auroral asymmetries in the two hemispheres [e.g., Østgaard *et al.*, 2005; Fillingim *et al.*, 2005] as the IMF modifies the ionospheric convection pattern leading to a hemispheric asymmetry in the intensity of field-aligned currents (FACs). Besides southward IMF B_z , the IMF B_y component is also considered to be an important driver of the FACs intensification. In particular, when IMF B_y is positive, there should be stronger upward FACs (Region 1) on the dusk side of the Southern Hemisphere [Kozlovsky *et al.*, 2003], and aurora should be brighter and more structured in the Southern Hemisphere [e.g., Fillingim *et al.*, 2005]. On the other hand, when the IMF B_x component dominates B_y , such conditions can lead to a more efficient solar wind dynamo and more intense Region 1 FACs in the Southern Hemisphere [e.g., Laundal and Østgaard, 2009; Reistad *et al.*, 2014].

During the main phase of the storm (17 March), the IMF orientation had a highly complex behavior. Three IMF components fluctuated several times between positive and negative values and vice versa. From ~06 to 11 UT, IMF positive B_x and negative B_y conditions dominated with peak values of 16.5 nT and -16.8 nT for B_x and B_y , respectively. During 11–15 UT with a new southward turn of B_z , the opposite situation with B_x and B_y domination occurred. B_x became negative, reaching a minimum value of -14 nT while the B_y component became positive, reaching a peak of 30 nT. After 15 UT, IMF B_y turned sharply to negative values, reaching -8 nT and then transitioned to positive values with a new peak of 20 nT around 18 UT. Large and rapid changes in B_x and B_y domination can lead to differences in FAC intensity in the Northern and Southern Hemispheres. As these changes had a rather short duration (few hours in UT), their possible impact on the ionospheric irregularities occurrence can be captured at different locations and MLTs by the diurnal maps constructed for the Northern and Southern Hemispheres (see Figure 3b). Besides the significant intensification of the large-scale FACs during severe geomagnetic storms, the impact of small-scale FACs can be also important to the generation of the ionospheric irregularities. For example, Park *et al.* [2012] reported that ionospheric irregularities observed by the CHAMP (Challenging Minisatellite Payload) satellite at high latitudes are generally accompanied by bursts of small-scale FACs, and they are related to Region 1 FACs. This question could be the subject of a future investigation involving FAC data products derived from Iridium or Swarm observations.

Acknowledgments

We acknowledge the use of the raw GPS data provided by IGS (<ftp://cddis.gsfc.nasa.gov>), UNAVCO (<ftp://data-out.unavco.org>), NOAA CORS (<ftp://geodesy.noaa.gov/cors>), EUREF (<ftp://rgpdata.ign.fr>), Natural Resources Canada (webapp.geod.nrcan.gc.ca), RAMSAC CORS of NGI of Argentina (www.igm.gov.ar/NuestrasActividades/Geodesia/Ramsac/), and Australian (<ftp://ftp.ga.gov.au>) and New Zealand (<ftp://geonet.org.nz>) GNSS networks. We also thank IGS and CODE for providing GPS products (orbits and biases). The authors thank the NASA/GSFC's Space Physics Data Facility's OMNIWeb service for providing OMNI data (<ftp://spdf.gsfc.nasa.gov/pub/data/omni>) and the program code for CGM coordinates calculation. The AE data are provided by the World Data Center for Geomagnetism, Kyoto University (wdc.kugi.kyoto-u.ac.jp). The HP data were provided by the Space Weather Prediction Center (SWPC) of NOAA (<http://www.swpc.noaa.gov/>). I.Z. was partially supported by the European Research Council (grant agreement 307998) and the RFB grant N15-35-20364. The authors thank two anonymous reviewers for their constructive comments, which improved greatly the interpretation of the results presented in this paper.

6. Summary and Conclusion

In this paper, we present features of the high-latitude ionospheric irregularities observed in GPS data during the 2015 St. Patrick's Day geomagnetic storm. We conclude that current fast-growing networks of GPS receivers can provide much more information about the ionospheric irregularities than it was possible for the past superstorms in the years 2003–2004. To the best of our knowledge, the diurnal and hourly ROTI maps for both Northern and Southern Hemispheres are presented here for the first time. The period of the most intense irregularities occurrence was strongly correlated with changes in the auroral HP index, and it was associated with processes related to enhanced auroral particle precipitation. The GPS-based results reveal interhemispheric differences in the ionospheric irregularities occurrence. We suggest that this asymmetry is related to the IMF orientation, which can lead to a hemispheric asymmetry in the Region 1 FACs. Formation and further evolution of SED and TOI structures caused the storm-induced plasma density gradients and the appearance of the strong GPS phase irregularities at the midlatitude and high latitude of the Northern Hemisphere. Significant increases in the intensity of irregularities within the polar cap were observed in both hemispheres associated with the formation and evolution of a polar tongue of ionization and polar cap patches. Further studies of the high-latitude ionosphere response to the St. Patrick's Day storm with the use of satellite and ground-based observations will be valuable for understanding processes within the ionosphere-magnetosphere system during geomagnetic storms.

References

- Aarons, J. (1997), Global Positioning System phase fluctuations at auroral latitudes, *J. Geophys. Res.*, *102*, 17,219–17,231, doi:10.1029/97JA01118.
- Astafyeva, E., Y. Yasyukevich, A. Maksikov, and I. Zhivetiev (2014), Geomagnetic storms, super-storms, and their impacts on GPS-based navigation systems, *Space Weather*, *12*, 508–525, doi:10.1002/2014SW001072.

- Blewitt, G. (1990), An automatic editing algorithm for GPS data, *Geophys. Res. Lett.*, *17*, 199–202, doi:10.1029/GL017i003p00199.
- Cherniak, I., A. Krankowski, and I. Zakharenkova (2014a), Observation of the ionospheric irregularities over the Northern Hemisphere: Methodology and service, *Radio Sci.*, *49*, 653–662, doi:10.1002/2014RS005433.
- Cherniak, I., I. Zakharenkova, and A. Krankowski (2014b), Approaches for modeling ionosphere irregularities based on the TEC rate index, *Earth Planets Space*, *66*(1), 165, doi:10.1186/s40623-014-0165-z.
- Coster, A., and A. Komjathy (2008), Space Weather and the Global Positioning System, *Space Weather*, *6*, S06D04, doi:10.1029/2008SW000400.
- Coster, A. J., and S. Skone (2009), Monitoring storm-enhanced density using IGS reference station data, *J. Geod.*, *83*(3–4), 345–351, doi:10.1007/s00190-008-0272-3.
- Coster, A. J., M. J. Colerico, J. C. Foster, W. Rideout, and F. Rich (2007), Longitude sector comparisons of storm enhanced density, *Geophys. Res. Lett.*, *34*, L18105, doi:10.1029/2007GL030682.
- Crowley, G., A. J. Ridley, D. Deist, S. Wing, D. J. Knipp, B. A. Emery, J. Foster, R. Heelis, M. Hairston, and B. W. Reinisch (2000), Transformation of high-latitude ionospheric F region patches into blobs during the March 21, 1990, storm, *J. Geophys. Res.*, *105*, 5215–5230, doi:10.1029/1999JA900357.
- Emery, B. A., V. Coumans, D. S. Evans, G. A. Germany, M. S. Greer, E. Holeman, K. Kadinsky-Cade, F. J. Rich, and W. Xu (2008), Seasonal, Kp, solar wind, and solar flux variations in long-term single-pass satellite estimates of electron and ion auroral hemispheric power, *J. Geophys. Res.*, *113*, A06311, doi:10.1029/2007JA012866.
- Fillingim, M. O., G. K. Parks, H. U. Frey, T. J. Immel, and S. B. Mende (2005), Hemispheric asymmetry of the afternoon electron aurora, *Geophys. Res. Lett.*, *32*, L03113, doi:10.1029/2004GL021635.
- Foster, J. C. (1993), Storm time plasma transport at middle and high latitudes, *J. Geophys. Res.*, *98*, 1675–1689, doi:10.1029/92JA02032.
- Foster, J. C., and W. J. Burke (2002), SAPS: A new categorization for sub-auroral electric fields, *Eos Trans. AGU*, *83*(36), 393–394, doi:10.1029/2002EO00289.
- Foster, J. C., et al. (2005), Multiradar observations of the polar tongue of ionization, *J. Geophys. Res.*, *110*, A09S31, doi:10.1029/2004JA010928.
- Fuller-Rowell, T. J., and D. S. Evans (1987), Height-integrated Pedersen and Hall conductivity patterns, *J. Geophys. Res.*, *92*, 7606–7618, doi:10.1029/JA092iA07p07606.
- GUIVIMED JHU/APL website (2015), [Available at guitimed.jhuapl.edu, guitimed.jhuapl.edu/guvi-images/guvi_aur.gif, Accessed 14 July.]
- Jakowski, N., V. Wilken, S. Schlueter, S. M. Stankov, and S. Heise (2005), Ionospheric space weather effects monitored by simultaneous ground and space based GNSS signals, *J. Atmos. Sol. Terr. Phys.*, *67*(12), 1074–1084, doi:10.1016/j.jastp.2005.02.023.
- Kamide, Y., and K. Kusano (2015), No major solar flares but the largest geomagnetic storm in the present solar cycle, *Space Weather*, *13*, 365–367, doi:10.1002/2015SW001213.
- Kersley, L., S. E. Pryse, I. K. Walker, J. A. T. Heaton, C. N. Mitchell, M. J. Williams, and C. A. Willson (1997), Imaging of electron density troughs by tomographic techniques, *Radio Sci.*, *32*, 1607–1621, doi:10.1029/97RS00310.
- Keskinen, M. J., and S. L. Ossakow (1983), Theories of high-latitude ionospheric irregularities: A review, *Radio Sci.*, *18*, 1077–1091, doi:10.1029/RS018i006p01077.
- Kintner, P. M., B. M. Ledvina, and E. R. De Paula (2007), GPS and ionospheric scintillations, *Space Weather*, *5*, S09003, doi:10.1029/2006SW000260.
- Kozlovsky, A., T. Turunen, A. Koustov, and G. Parks (2003), IMF By effects in the magnetospheric convection on closed magnetic field lines, *Geophys. Res. Lett.*, *30*(24), 2261, doi:10.1029/2003GL018457.
- Laundal, K. M., and N. Østgaard (2009), Asymmetric auroral intensities in the Earth's Northern and Southern Hemispheres, *Nature*, *460*(7254), 491–493, doi:10.1038/nature08154.
- Newell, P. T., T. Sotirelis, K. Liou, C.-I. Meng, and F. J. Rich (2007), A nearly universal solar wind-magnetosphere coupling function inferred from 10 magnetospheric state variables, *J. Geophys. Res.*, *112*, A01206, doi:10.1029/2006JA012015.
- Newell, P. T., T. Sotirelis, and S. Wing (2009), Diffuse, monoenergetic, and broadband aurora: The global precipitation budget, *J. Geophys. Res.*, *114*, A09207, doi:10.1029/2009JA014326.
- Newell, P. T., T. Sotirelis, K. Liou, A. R. Lee, S. Wing, J. Green, and R. J. Redmon (2010), Predictive ability of four auroral precipitation models as evaluated using Polar UVI global images, *Space Weather*, *8*, S12004, doi:10.1029/2010SW000604.
- Nishitani, N., T. Hori, R. Kataoka, Y. Ebihara, and K. Shiokawa (2015), Characteristics of ionospheric convection associated with low-latitude aurora observed at Rikubetsu, Hokkaido during the 2015 March storm, Abstract presented at SuperDARN workshop 2015, Leicester, U. K. [Available at <http://www2.le.ac.uk/departments/physics/research/rssp/sd/superdarn-2015/superdarn-workshop-2015-programme/superdarn-workshop-2015-abstracts>.]
- Østgaard, N., N. A. Tsyganenko, S. B. Mende, H. U. Frey, T. J. Immel, M. Fillingim, L. A. Frank, and J. B. Sigwarth (2005), Observations and model predictions of substorm auroral asymmetries in the conjugate hemispheres, *Geophys. Res. Lett.*, *32*, L05111, doi:10.1029/2004GL022166.
- Park, J., R. Ehrlich, H. Lühr, and P. Ritter (2012), Plasma irregularities in the high-latitude ionospheric F-region and their diamagnetic signatures as observed by CHAMP, *J. Geophys. Res.*, *117*, A10322, doi:10.1029/2012JA018166.
- Phelps, A. D. R., and R. C. Sagalyn (1976), Plasma density irregularities in the high-latitude top side ionosphere, *J. Geophys. Res.*, *81*, 515–523, doi:10.1029/JA081i004p00515.
- Pi, X., A. J. Mannucci, U. J. Lindqwister, and C. M. Ho (1997), Monitoring of global ionospheric irregularities using the worldwide GPS network, *Geophys. Res. Lett.*, *24*, 2283–2286, doi:10.1029/97GL02273.
- Prikryl, P., P. T. Jayachandran, S. C. Mushini, D. Pokhotelov, J. W. MacDougall, E. Donovan, E. Spanswick, and J. P. St.-Maurice (2010), GPS TEC, scintillation and cycle slips observed at high latitudes during solar minimum, *Ann. Geophys.*, *28*(6), 1307–1316, doi:10.5194/angeo-28-1307-2010.
- Reistad, J. P., N. Østgaard, K. M. Laundal, S. Haaland, P. Tenfjord, K. Snekvik, K. Oksavik, and S. E. Milan (2014), Intensity asymmetries in the dusk sector of the poleward auroral oval due to IMF Bx, *J. Geophys. Res. Space Physics*, *119*, 9497–9507, doi:10.1002/2014JA020216.
- Rodger, A. S., R. J. Moffett, and S. Quegan (1992), The role of ion drift in the formation of ionisation troughs in the mid- and high-latitude ionosphere—A review, *J. Atmos. Terr. Phys.*, *54*(1), 1–30.
- Skone, S., and R. Yousuf (2007), Performance of satellite-based navigation for marine users during ionospheric disturbances, *Space Weather*, *5*, S01006, doi:10.1029/2006SW000246.
- Smith, A. M., C. N. Mitchell, R. J. Watson, R. W. Meggs, P. M. Kintner, K. Kauristie, and F. Honary (2008), GPS scintillation in the high arctic associated with an auroral arc, *Space Weather*, *6*, S03D01, doi:10.1029/2007SW000349.
- Sojka, J. J., M. D. Bowline, R. W. Schunk, D. T. Decker, C. E. Valladares, R. Sheehan, D. A. Anderson, and R. A. Heelis (1993), Modeling polar cap F-region patches using time varying convection, *Geophys. Res. Lett.*, *20*, 1783–1786, doi:10.1029/93GL01347.

- Tiwari, R., H. J. Strangeways, S. Tiwari, and A. Ahmed (2013), Investigation of ionospheric irregularities and scintillation using TEC at high latitude, *Adv. Space Res.*, *52*(6), 1111–1124, doi:10.1016/j.asr.2013.06.010.
- Tsunoda, R. T. (1988), High-latitude F region irregularities: A review and synthesis, *Rev. Geophys.*, *26*, 719–760, doi:10.1029/RG026i004p00719.
- U.S. Geological Survey (2015), National Geomagnetism Program. [Available at <http://geomag.usgs.gov/storm/22>, Accessed 14 July.]
- Wanner, B. (2015), DR #127: Effect on WAAS from Iono Activity on March 17–18, 2015, WAAS Technical Report, WAAS Test Team. [Available at <http://www.nstb.tc.faa.gov/Discrepancy%20Reports%20PDF/DR%20127%20Effect%20on%20WAAS%20from%20Iono%20Activity%20March%2017%202015.pdf>, Accessed 14 July.]
- Zakharenkova, I. E., I. V. Cherniak, A. Krankowski, and I. I. Shagimuratov (2014), Vertical TEC representation by IRI 2012 and IRI Plas models for European midlatitudes, *Adv. Space Res.*, *55*(8), 2070–2076, doi:10.1016/j.asr.2014.07.027.